COUPLED HYDROMECHANICAL MODELING OF INDUCED SEISMICITY FROM CO_2 INJECTION IN THE ILLINOIS BASIN

Keurfon Luu[1*], Martin Schoenball[1, 2], Curtis M. Oldenburg[1], and Jonny Rutqvist[1]

[1]Energy Geosciences Division, Lawrence Berkeley National Laboratory, Berkeley, CA, USA

Email: keurfonluu@lbl.gov, jrutqvist@lbl.gov, cmoldenburg@lbl.gov

[2]now at Nagra, Wettingen, Switzerland

Email: martin.schoenball@nagra.ch

To be submitted to Journal of Geophysical Research: Solid Earth

(*) Corresponding author

Abstract

Injection of CO_2 for geologic carbon sequestration (GCS) into deep sedimentary formations involves fluid pressure increases that engage hydromechanical processes that can cause seismicity by activation of existing faults. In this work, we use a coupled multiphase fluid flow and geomechanical simulator to model spatiotemporal fluid pressure and stress changes in order to study the poroelastic effect of CO_2 injection on faults in crystalline basement rock below the injection zone. The seismicity rate along features interpreted to be basement faults is modeled using Dieterich's rate-and-state earthquake nucleation model. The methodology is applied to microseismicity detected during CO_2 injection into the Mount Simon formation during the Illinois Basin – Decatur Project. The modeling accurately captures an observed reduction in seismicity rate when the injection in the second well was into a slightly shallower zone above the base of the Mount Simon formation. Moreover, the modeling shows that it is important to consider poroelastic stress changes, in addition to fluid pressure changes for accurately modeling of the observed seismicity rate.

Keywords: geomechanics; induced seismicity; geologic carbon sequestration; modeling; Illinois Basin, Mount Simon

1. Introduction

One contemporary critical challenge is to significantly mitigate emissions of greenhouse gases in order to prevent a dramatic global climate change. In the last decades, geological carbon sequestration (GCS) has been investigated as one possible solution to reduce emissions of carbon dioxide (CO_2) into the atmosphere (Benson and Cole, 2008). GCS consists in injecting captured CO_2 into deep subsurface geological reservoirs such as deep saline aquifers or depleted oil and gas fields (Celia, 2017; Metz et al., 2005).

The underground injection of large volumes of CO_2 causes pressure rise that results in geomechanical strain and stress changes within and surrounding the

targeted storage formation (Rutqvist, 2012). Activation of pre-existing fractures and faults may be an issue of concern for the potential of inducing seismicity that could be felt by humans on the ground surface or for the potential of opening up a new flow path through an overlying caprock (Rutqvist, 2012; Rutqvist et al., 2016; Vilarrasa et al., 2019; M. D. Zoback and Gorelick, 2012). In this context the concept of fractures and faults in the host rock being near critically stressed for activation by shear slip is relevant (Zoback and Zoback, 1989). It means that a small change in reservoir pressure by injection may be sufficient to trigger activation of pre-existing faults and cause seismic events.

Although no significant seismic event induced by CO_2 injection has occurred at any GCS site to date, it is necessary to understand whether industrial scale sequestration can lead to seismic events of magnitudes that can be perceived by humans. Indeed, a felt seismic event could potentially lead to the abandonment of a project as it has been the case in some geothermal projects (e.g., Deichmann and Giardini, 2009).

Events of significant magnitude have been associated with wastewater injection in the United States mid-continent region (Weingarten et al., 2015). Seismicity in these areas has been attributed to basement faults triggered by wastewater injection into deep reservoirs close to crystalline basement rock. Seismicity has been inferred to be triggered by very small pressure changes indicating activation of faults that are critically stressed (i.e., close to instability) (Hombach et al., 2015; Keranen et al., 2014).

The potential for fault activation and induced seismicity associated with underground fluid injection during GCS activities, has been the subject of a number of modeling studies in recent years (Cappa and Rutqvist, 2011; Jha and Juanes, 2014; Rutqvist et al., 2016; Vilarrasa et al., 2019). Fault reactivation mechanisms involve complex coupled physical processes that are still not fully understood, but it is generally acknowledged that the first-order cause of injection-induced fault reactivation is changes in pore pressure which reduce the shear strength of optimally oriented faults and bring them closer to the point of failure where classical Mohr-Coulomb failure criteria is used to characterize the susceptibility of faults to slip.

With the recent surge in seismicity attributed to anthropic activities in United States mid-continent, post-mortem numerical modeling studies serve to increase understanding of the mechanisms underlying induced seismicity (Choy et al., 2016; Ellsworth et al., 2015). Most studies assume that fault reactivation is primarily driven by pore pressure diffusion and thus neglect injection-induced poroelastic stress changes. However, several recent numerical studies indicate that poroelastic effects must be captured by numerical models in order to correctly forecast fluid-induced seismicity (Barbour et al., 2017; Zhai et al., 2019). Most of these studies are related to wastewater injection or enhanced geothermal systems (Barbour et al., 2017; Hakimhashemi et al., 2014; Norbeck and Rubinstein, 2018), while only a handful of sites reported fluid-induced microseismicity (i.e., $M_w < 2$, not felt by humans) associated with CO_2 injection, namely at

In Salah, Algeria (Rutqvist et al., 2016; Verdon et al., 2015); Otway, Australia (Myer and Daley, 2011; Siggins, 2010), and the Illinois Basin – Decatur Project (IBDP), United States (Bauer et al., 2016; Kaven et al., 2015; Will et al., 2016).

The IBDP is the first carbon capture and sequestration project in the United States that injected commercial volumes of CO_2 into a deep saline aquifer for GCS (Finley, 2014). One million tons of CO_2 was injected over a 3-year injection period from November 2011 to November 2014 at the well CCS1 into a high permeability Mount Simon Sandstone interval at a depth of around 2140 m. Nearly 20,000 induced microseismic events were detected with most events located within the underlying crystalline Precambrian basement (Williams-Stroud et al., 2020). Identified clusters of microseismic events form semilinear features oriented within 30° of the direction of the maximum horizontal principal stress (azimuth N068°) and indicate that the seismicity at the IBDP is occurring along pre-existing basement faults (Goertz-Allmann et al., 2017). In April 2017, CO_2 started to be injected in the CCS2 well in a zone less than 50 m shallower than the injection zone in the CCS1 well. Injection was into the Lower Mount Simon in both wells, but with a higher injection rate in the CCS2 well compared to that of CCS1. Yet, there is very little microseismicity occurring during injection into CCS2 (Williams-Stroud et al., 2020).

Here, we demonstrate an approach for modeling the induced seismicity observed at the IBDP along basement faults using multiphase fluid flow and geomechanical model simulations coupled with a rate-and-state nucleation model. The organization of the paper is as follows: In Section 2, we describe the computational model used in this study. In Section 3.1, we show the result of the earthquake catalog declustering that is used to calibrate the rate-and-state parameters in Section 3.2. The modeling results for both injections in wells CCS1 and CCS2 are then detailed in Section 3.3. Finally, we use our model to study the effect of varying injection scenarios on predicted induced seismicity in Section 3.4.

1. **Numerical model**

In this work, we consider a three-dimensional domain that includes discretized faults within the basement inferred from the microseismic clusters observed at the IBDP site. We simulate the CO_2 injection and stress evolution using the coupled multiphase flow and geomechanical model and apply the rate-and-state seismicity model to study the response of the basement faults to the CO_2 injection.

1. **Computational model**

We consider a simplified version of the subsurface structure at the Decatur site with a three-dimensional layer-cake model geometry consisting of ten homogeneous geological layers with the top layer representing the primary seal Eau Claire formation (1540 m depth below ground surface (bgs)) and the bottom layer representing the crystalline basement (2100 to 3000 m bgs) (Bauer et al., 2016). The Mount Simon sandstone formation is divided into six different lay-

ers in the model, representing from bottom to top, the Lower Mount Simon A – lower zone, Lower Mount Simon A – upper zone, and the Mount Simon B, C, D, and E zones. The injection interval is located in the Mount Simon A – lower zone which has been divided into three sublayers to improve flow modeling within the reservoir. A thin continuous mudstone layer is included to honor multilevel pressure data recorded at the IBDP site which shows that vertical migration of the CO_2 plume that formed after injection into CCS1 is limited by discontinuous low-permeability layers that inhibit vertical fluid flow within the reservoir (Senel et al., 2014; Strandli et al., 2014; Williams-Stroud et al., 2020). Hydromechanical properties of the geological layers are summarized in Table 1.

Sixteen microseismic clusters are identified using the DBSCAN algorithm (Ester et al., 1996) and used to map faults in our model. Faults are discretized as finite-thickness elements within the basement and are displayed in Figure 1 (middle). All faults are about 20 m thick and uniform in properties (i.e., fault core is not distinguished from damage zone). A detailed microseismic analysis showed that the basement faults at Decatur are hydraulically connected to the reservoir (Goertz-Allmann et al., 2017). Therefore, the faults discretized in our model vertically extend from the bottom of the reservoir (2146 m) to the bottom of the model (3000 m). We consider the faults to be hydraulically conductive with permeability logarithmically decreasing with depth from 1 mD at the top (2146 m) to 0.1 mD at the bottom (3000 m). This type of permeability variation has been reported to be associated with critically stressed crystalline basement faults (Barbour et al., 2017; Townend & Zoback, 2000). For the sake of simplicity, we consider that all faults are vertical (dip angle $\theta = 90^\circ$) and have the same elastic properties as the host rock units they transect (i.e., only the permeability of faults are different).

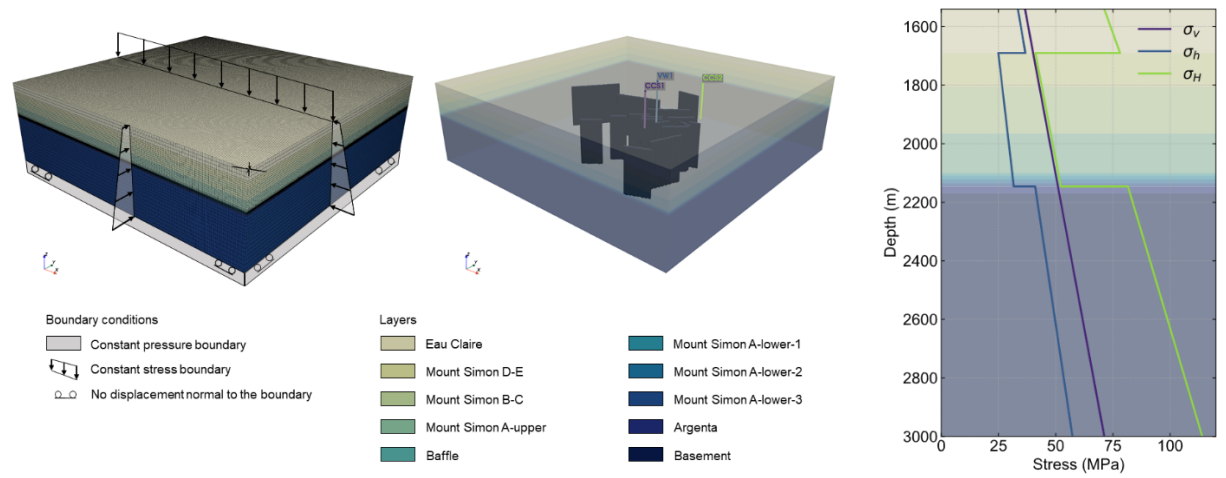

Figure 1. (Left-hand side) Computational mesh and boundary conditions. (Middle) Faults discretized within the model and well locations. (Right-hand side) Initial stress conditions.

Table 1. Hydromechanical properties of model layers. Reservoir hydrological properties are history-matched against pressure transient and saturation data recorded at verification well VW1 and mechanical properties are estimated from well logs (see Appendix A for details).

Layer	Top (depth bgs) (m)	(kg/m^3)	K_h (mD)	K_v (mD)	C_p (GPa^{-1})	V_p (km/s)	V_s (km/s)	E (GPa)	(-)	(-)
Eau Claire			10^{-5}	10^{-5}						
Mount Simon D-E										
Mount Simon B-C										
Mount Simon A-upper										
Baffle										
Mount Simon A-lower-1										
Mount Simon A-lower-2										

Layer	Top (depth bgs) (m)	(kg/m^3)	K_h (mD)	K_v (mD)	C_p (GPa^{-1})	V_p (km/s)	V_s (km/s)	E (GPa)	(-)	(-)
Mount Simon A-lower-3										
Argenta Basement			-4	-4						

Figure 1 (left-hand side) shows the computational mesh with the applied boundary conditions. The mesh consists of 200 x 200 x 50 (2 million) hexahedral elements uniformly discretized horizontally and refined vertically in the vicinity of the injection zone. Lateral and bottom boundaries are open to fluid flow with only the top boundary being closed to flow. We apply fixed stress conditions at lateral and top boundaries, and rollers at the bottom (no vertical displacement). Following Senel et al. (2014), we assume an initial hydrostatic gradient for pore pressure (10.15 MPa/km) and vertical geothermal gradient for temperature (18.2 $^\circ$C/km). The system is initially 100% brine-saturated with salinity of 20% and hydrostatic initial fluid pressure. Initial in-situ stress conditions are defined according to Bauer et al. (2016) and correspond to a strike-slip faulting system with $\sigma_H > \sigma_v > \sigma_h$ (Figure 1, right-hand side). In-situ stress measurements show that the maximum horizontal stress direction has a fairly constant azimuth and is oriented N068° (Bauer et al., 2016; Williams-Stroud et al., 2020). The minimum horizontal stress gradient in each formation is estimated based on measurements, whereas the maximum horizontal stress gradient is calculated assuming that the host rock is near critically stressed conditions for instability for a friction coefficient $\mu = 0.6$.

Figure 2 shows capillary pressure and relative permeability curves used in the multiphase fluid flow simulation. We follow Mehnert et al. (2019) and use van Genuchten capillary pressure model (Genuchten, 1980) with fitting parameter $\lambda = 0.55$, residual liquid saturation $S_{\mathrm{lr}} = 0.6$, saturated liquid content $S_{\mathrm{ls}} = 0.999$ and maximum capillary pressure $P_{\mathrm{max}} = 6.9$ MPa. Relative permeability curves are constructed using the van Genuchten-Mualem model with fitting parameter $\lambda = 1.36$, residual liquid saturation $S_{\mathrm{lr}} = 0.65$ and residual gas saturation $S_{\mathrm{gr}} = 0.01$.

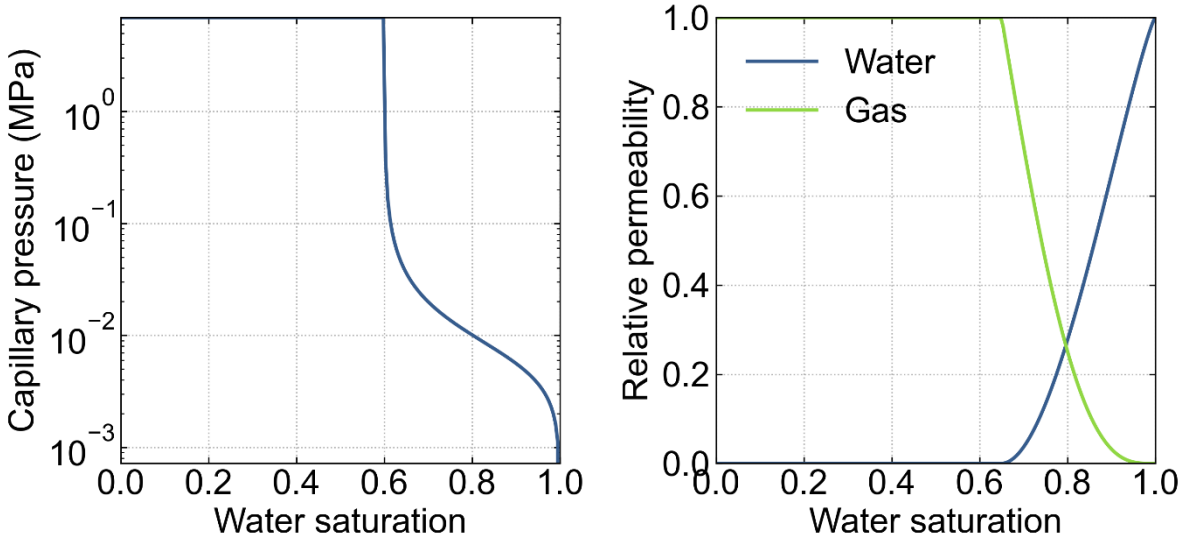

Figure 2. Capillary pressure (left-hand side) and relative permeability curves (right-hand side).

For simplicity, all coordinates shown in this work are relative to injection well CCS1 (i.e., well CCS1 is located at $x = y = 0$ m and its top is at $z = 0$ m).

1. **Seismicity rate modeling**

   (a) **Rate-and-state seismicity model**

We model the seismicity rate using a hybrid approach where seismicity rate is calculated from time-dependent pressure and stress changes simulated by our coupled hydromechanical model (Hakimhashemi et al., 2014). We use Dieterich's rate-and-state earthquake nucleation model to assess the evolution of seismicity rate due to injection-induced stress changes along basement faults (Dieterich, 1994). The rate-and-state seismicity model estimates the number of independent events in response to a change in stress on a set of faults and is described by the following ordinary differential equation (Dieterich, 1994; Segall and Lu, 2015)

$$\frac{\mathrm{dR}}{\mathrm{dt}} = \frac{R}{t_c}\left(\frac{\dot{\tau}}{\dot{\tau_0}} - R\right) \quad (1)$$

where $R = \frac{r}{r_0}$ is the seismicity rate r relative to the background rate r_0, $t_c = \frac{\mathrm{A}}{\dot{\tau_0}}$ is the characteristic relaxation time, $\dot{\tau}$ and $\dot{\tau_0}$ are the Coulomb and background stressing rates, respectively. We solve the ordinary differential equation using a fifth-order adaptive time step Runge-Kutta-Fehlberg algorithm (Fehlberg, 1969) with a relative error tolerance $\epsilon_r = 10^{-6}$.

We note that the rate-and-state seismicity model is only applicable if optimally

oriented faults are already critically stressed prior to injection (Chang and Segall, 2016; Zhai et al., 2019). In addition, the theory only relates to earthquake nucleations (mainshocks) and does not account for the physical processes involved in aftershock sequences. More specifically, while the geomechanical model accounts for stress transfer from injection pressure changes and poroelastic stress propagating ahead of the pressure front, stress changes induced by seismic slip of individual fractures or faults that can trigger another event are not included. Thus, earthquake catalogs must be declustered (removal of aftershocks) to be able to compare observed seismicity rates with results of the rate-and-state model. This model limitation also implies that it does not forecast magnitudes of earthquakes. However, physics-based seismicity-rate models can be combined with the Gutenberg-Richter law to calculate the probability of occurrence of an earthquake of magnitude M (Navas-Portella et al., 2020; Segall and Lu, 2015). For magnitudes $M > M_{\min}$, the total number of events at time step t is defined as

$$R(t,\ M) = r_0 \left(b \log 10\right) 10^{-b(M - M_{\min})} R(t) \quad (2)$$

with b being the b-value. The number of earthquakes in time interval $[t_1,\ t_2]$ is written

$$N\left(t_1,\ t_2\right) = \int_{t_1}^{t_2} \int_{M_{\min}}^{M_{\max}} R(t,\ M) \mathrm{dMdt} \quad (3)$$

where $M_{\min}$ and $M_{\max}$ are the minimum and maximum magnitudes simulated. In the following, $M_{\min}$ is set to the catalog's magnitude of completeness and $M_{\max}$ is chosen sufficiently large. Assuming that earthquake occurrence is described by a inhomogeneous Poissonian process, Zhai et al. (2020) estimates the magnitude probability of exceedance (i.e., the probability of having at least one event of magnitude larger than M) following

$$P_{\geq M}\left(t_1,\ t_2\right) = 1 - exp\left(N_{\geq M}\left(t_1,\ t_2\right)\right) \quad (4)$$

where $N_{\geq M}\left(t_1,\ t_2\right)$ is the expected number of earthquakes with magnitude greater than or equal to M.

1. **Stressing rate modeling**

Dieterich's rate-and-state seismicity model relates changes in Coulomb stress to changes in seismicity rate. We define the Coulomb stressing rate as the change in Coulomb stress ΔCFS per unit of time which is calculated at each time step of the simulation following

$$\Delta CFS = \Delta\tau_s + \mu\left(\Delta\sigma_n + \Delta P\right) \quad (5)$$

where μ is the friction coefficient (assumed to be 0.6 for all faults), $\Delta\tau_s$ is the change in shear stress, $\Delta\sigma_n$ is the change in normal stress (positive for tension), and ΔP is the change in fluid pressure. Shear stress τ_s and normal stress σ_n acting on a fault plane can be calculated from the stress tensor following

$$\begin{cases} \tau_s = \left(\| \cdot \mathbf{n} \|^2 - \sigma_n^2 \right)^{\frac{1}{2}} \\ \sigma_n = \mathbf{n} \cdot \cdot \mathbf{n} \end{cases} \quad (6)$$

where $\mathbf{n}$ is the normal vector of a given fault plane and $\|\cdot\|$ denotes the Euclidean norm.

We simulate the spatiotemporal distributions of fluid pressure, shear, and normal stresses using the latest version of the coupled fluid flow and geomechanical software TOUGH-FLAC (Rutqvist et al., 2002; Rutqvist, 2011) that sequentially couples the finite-volume multiphase flow simulator TOUGH3 (Jung et al., 2017) and the commercial finite-difference geomechanical software FLAC3D V7. The latest version of TOUGH-FLAC (Rinaldi et al., 2021) integrates all the new features of TOUGH3, in particular the use of PETSc parallel solvers which allows execution of coupled simulations with a large number of grid blocks (here, 2 million elements). By the use of TOUGH-FLAC, we account for full hydromechanical coupling with porosity changes modeled as a function of bulk modulus and volumetric strain. Fluid pressure and stresses are calculated at discrete time steps controlled by TOUGH3 using adaptive time stepping based on the number of Newton-Raphson iterations needed for each time step. However, we set the maximum time-step size to three days to better capture amplitudes of pressure changes due to the numerous shut-in phases. We further fit cubic splines to the simulated pressures and stresses which are used to calculate the changes in Coulomb stress ΔCFS. Finally, the stressing rate $\dot{\tau}$ is taken as the numerical time derivative of ΔCFS with a time step size $dt = 1$ day, following

$$\dot{\tau} = \frac{d\Delta\mathrm{CFS}}{\mathrm{dt}} \quad (7)$$

The coupled hydromechanical model generates spatial and temporal distributions of pressure and stress in the whole model. However, we assume that seismicity occurs only along pre-existing critically stressed faults and therefore only calculate Coulomb stress changes at integration points corresponding to the finite-thickness fault elements.

1. **Results**

We apply our coupled hydromechanical rate-and-state nucleation model to generate seismicity forecasts for both injections in wells CCS1 and CCS2. Modeled seismicity, especially for the first injection during which most of the seismicity is observed, is compared to the declustered catalog.

1. **Catalog declustering**

At the IBDP, more than 5,000 microseismic events have been located with magnitudes ranging from -2.1 to 1.2, and the magnitude of completeness is $M_c = -0.7$ (Goertz-Allmann et al., 2017; Williams-Stroud et al., 2020). Earthquake catalogs usually contain independent earthquakes (mainshocks) and earthquakes resulting from stress release after a mainshock (aftershocks). As explained in Section 2.2.2, the rate-and-state theory mainly focuses on the mainshocks and therefore aftershocks must be removed from the catalog to compare the hy-

brid seismicity model with observed seismicity. We consider a complete catalog and remove events with magnitudes lower than the magnitude of completeness ($M < -0.7$). We decluster the earthquake catalog using the nearest-neighbor method (Zaliapin and Ben-Zion, 2020). By this approach, for each earthquake in the catalog, we calculate the nearest-neighbor interevent distance in the space-time-magnitude domain. Given a pair of events i and j, the nearest-neighbor η_{ij} is calculated following

$$\eta_{ij} = R_{ij} T_{ij} \quad (8)$$

where R_{ij} and T_{ij} are the rescaled time and distance, respectively, written

$$\begin{cases} R_{ij} = (r_{ij})^d \, 10^{-wm_i/2} \\ T_{ij} = t_{ij} 10^{-wm_i/2} \end{cases} \quad (9)$$

with r_{ij} is the Euclidean interevent distance, t_{ij} the interevent time, d the fractal dimension of earthquake epicenter, w a weighting coefficient, and m_i the magnitude of event i. In this paper, we followed Zaliapin and Ben-Zion (2020) and set $d = 1.5$ and $w = 0$ (i.e., earthquakes' depths and magnitudes are not considered for the declustering).

Figure 3 shows the 2D distributions of calculated nearest-neighbor distance for the full (left-hand side) and declustered (right-hand side) catalogs. An earthquake that yields a low distance is close in space and time to its nearest-neighbor and is thus discriminated as an aftershock.

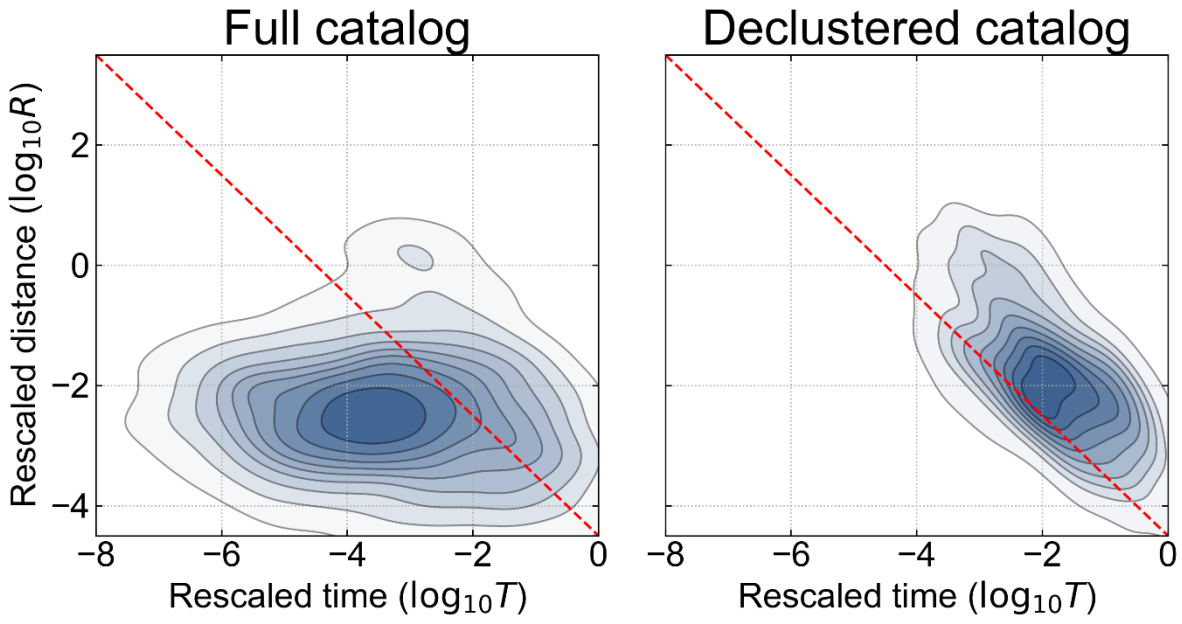

Figure 3. 2D distributions of nearest-neighbor distances for the full catalog (left-hand side) and declustered catalog (right-hand side). The red dashed line corresponds to the initial cutoff threshold η_0 used for the declustering.

It should be mentioned that declustering algorithms are usually tailored to remove aftershocks in natural earthquake catalogs. Nevertheless, the bimodality of the nearest-neighbor distribution has been observed in induced earthquake sequences (Schoenball et al., 2015; Schoenball and Ellsworth, 2017).

1. **Parameter calibration**

The rate-and-state seismicity model is governed by three parameters, namely the background stressing rate, the background seismicity rate and a constitutive parameter A that controls the characteristic relaxation time. The background stressing rate is usually obtained through geodetic measurements and the background seismicity rate can be estimated by monitoring the seismicity prior to the injection. We use a background stressing rate of $\dot{\tau_0} = 5$ Pa/year as estimated for the Southern Illinois Basin (Hamburger et al., 2010). Continuous microseismic monitoring has been carried out at the IBDP site prior to the first injection during 18 months and eight earthquakes with magnitude $M < -1.5$ were interpreted as local events (Smith and Jaques, 2016). Because of the lack of recorded natural earthquakes with magnitude $M \geq -0.7$ in the area of study, we calibrate the background seismicity rate r_0 along with the parameter A by manually fitting the modeled cumulative number of events during the first injection to the observed one (Hakimhashemi et al., 2014). We use a global optimization algorithm, namely the CMA-ES (Hansen and Ostermeier, 2001), to further refine the two parameters with a population size of 20 for the evolutionary algorithm, a maximum of 100 iterations and the manually calibrated parameters as initial mean. Eventually, we found a background seismicity rate $r_0 = 0.375$ events/year ($M \geq -0.7$) and $A\sigma = 0.032$ MPa. It should be mentioned that the background seismicity rate is estimated so that model outputs (relative to background seismicity) can be compared with the declustered catalog. The calibrated value of the background seismicity rate is fairly uncertain (see SI, Section S1). Figure 4 shows the calibration result displayed against the observed cumulative number of events.

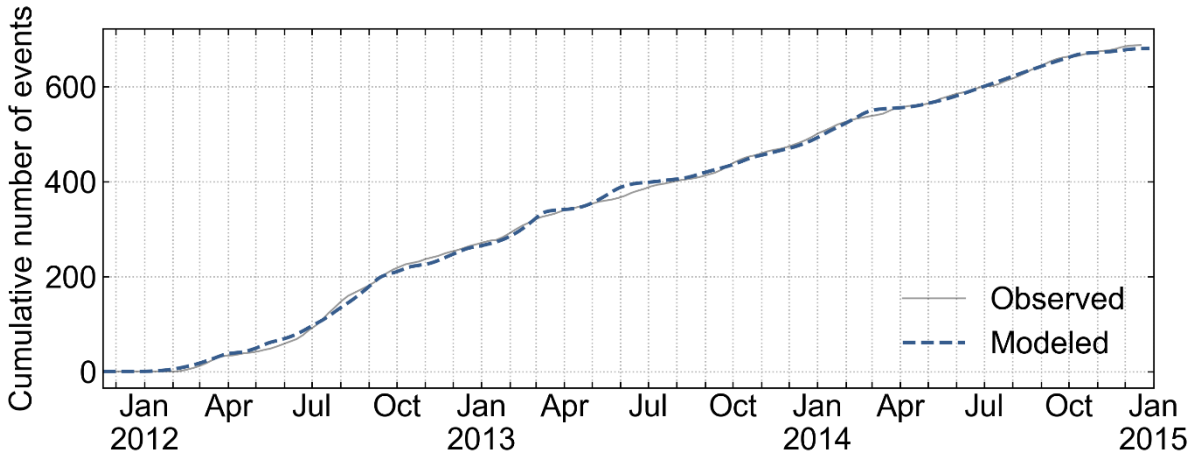

Figure 4. Cumulative number of events ($M \geq -0.7$) during the first injection in well CCS1. The gray solid line and the blue dashed line represent the observed and modeled cumulative numbers of events, respectively.

1. **Seismicity induced by injection in wells CCS1 and CCS2**

Figure 5 shows the modeled seismicity rate considering both injections in wells CCS1 (from November 2011 to November 2014) and CCS2 (from April 2017 to April 2018). To model the first injection, we inject CO_2 below a low permeability mudstone layer simplified in the model to represent the discontinuous baffles in the Mount Simon that restrict vertical flow. The two perforated zones (2121 m and 2129 m bgs) are modeled as single injection element. For the second injection, CO_2 is injected above the low permeability layer 50 m shallower (2178 m bgs) compared to the first injection. We note that only the first year of the second injection is modeled. Overall, the modeled seismicity rate follows the average behavior of the observed seismicity rate. More specifically, the modeled seismicity rate is consistent with the declustered catalog in terms of onset timings and peak rate amplitudes for the first injection, which means that the model is able to reproduce the main temporal features of the earthquake sequence. We observe that many of the longest shut-in phases (e.g., September 2012, March 2013, February 2014, October 2014) yield a sharp decrease in the modeled seismicity rate which indicates that the modeled seismicity rate and the injection rate are correlated. After the end of the injection in well CCS1, the modeled seismicity rate progressively decreases and predicts a lower rate than the background seismicity from July 2015 due to negative stressing rates. Despite larger injection rates in well CCS2 (1.7 times the injection rate in well CCS1), the modeled seismicity rate is negligible compared to the seismicity induced by the first injection (about two orders of magnitude smaller in seismicity rate).

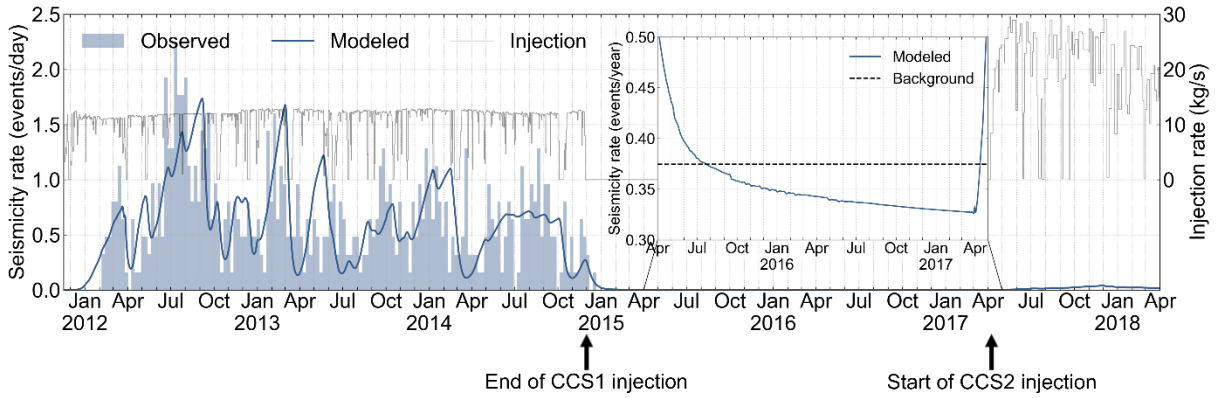

Figure 5. Modeled seismicity rate (blue solid line) compared with the declustered catalog (blue bars). The injection rate is represented by the thin gray solid line. The inset shows the same data at increased scale (we note the difference in unit for the y-axis).

The 2D spatial and temporal distributions of the modeled seismicity rate for the first injection are shown in Figure 6. These seismicity rate maps are obtained by integrating the modeled seismicity rate with respect to depth. The maps are then further smoothed by applying a Gaussian filter with a correlation length of 40 m to improve the readability of the figure. Seismicity rate maps are generated every six months starting from January 2012. The modeled seismicity rate largely replicates the principal features of the observed seismicity, with several discrepancies likely due to the limitations and assumptions used for our modeling. For instance, the model forecasts an increase in seismicity in the vicinity of the injection well CCS1 in 2014 although only few earthquakes have been observed in this area in that time period. This may be due to the lack of heterogeneity in the hydromechanical model which results in a rather symmetrical pressurization of the reservoir around the injection well.

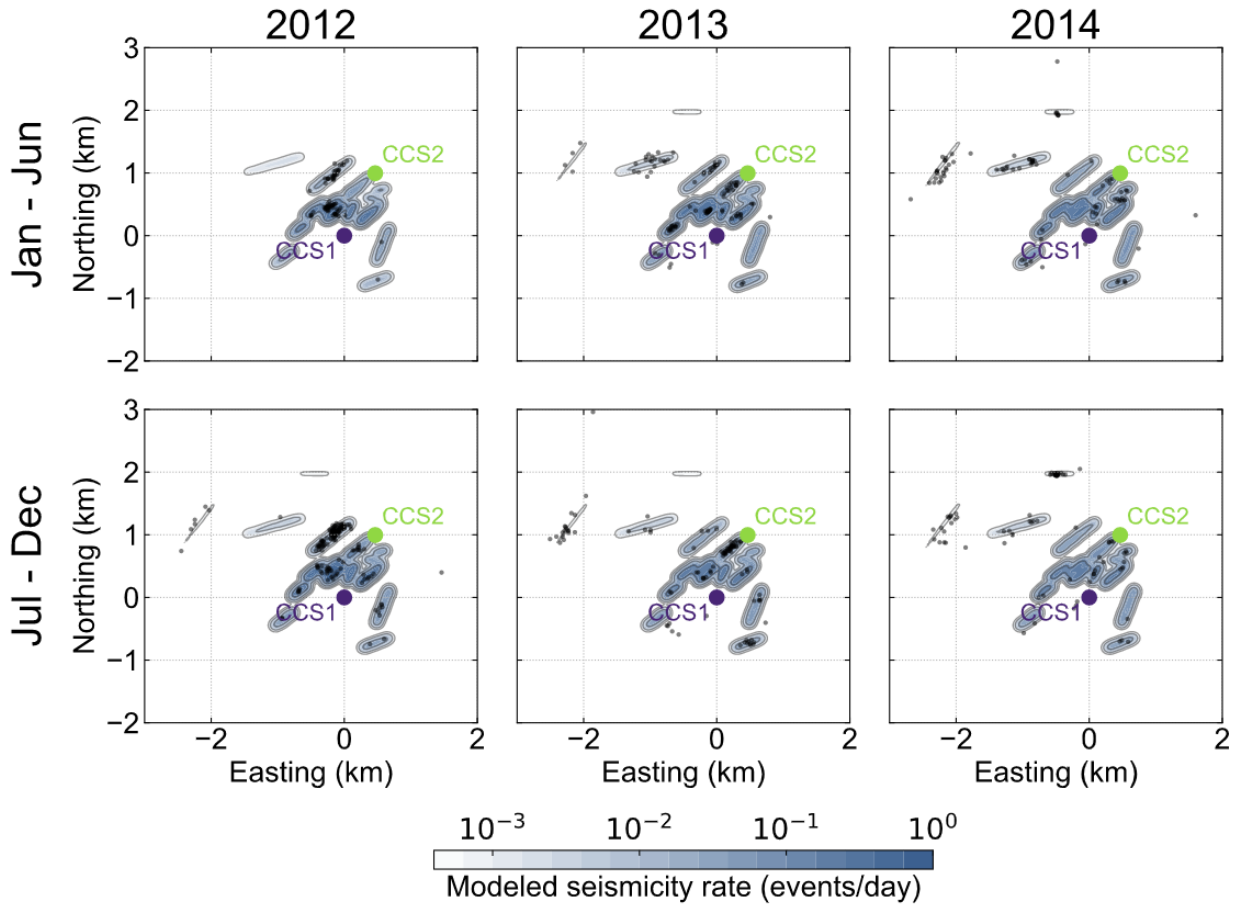

Figure 6. Seismicity rate maps. The black dots indicate the earthquake epicenters from the declustered catalog ($M \geq -0.7$).

We further investigate the relative contributions of pressure and injection-induced stress changes to the Coulomb stress by tracking their evolutions at different points throughout the model. According to Equation 5, contribution to the Coulomb stress changes are changes in shear stress $\Delta\tau_s$, changes in normal stress $\Delta\sigma_n$ and changes in fluid pressure ΔP. The changes in shear stress and normal stress are induced by poroelastic stresses in the system that are in turn due to injection-induced pressure changes in the system. In the following, we define ΔP as the pressure contribution and terms $\Delta\tau_s + \Delta P$ of Equation 5 as poroelastic contribution to the Coulomb stress change. To monitor the evolution of the pressure and poroelastic stress to the Coulomb stress, we select a first point midway between wells CCS1 and CCS2 to study the near-field, and a second point on the westernmost fault for the far-field. For both points, we display in Figure 7 the evolution of the Coulomb stress change (black) along with the contribution from pore pressure (purple) and poroelastic

stress (green) changes at different depths (2200 m, 2400 m, and 2600 m bgs). Poroelastic stress effects are not negligible at the top of the basement in the near-field (upper left plot) and seem to impede reactivation by reducing the changes in Coulomb stress as $\Delta CFS < \mu\Delta P$. However, farther from the reservoir, we have $\Delta\tau_s + \mu\Delta\sigma_n \approx 0$ and $\Delta CFS \approx \mu\Delta P$, which indicates that the poroelastic stress impact decreases with depth where direct pressure effects become dominant. The modeled relative seismicity rates at the selected points are also shown in Figure 7 on a logarithmic scale (blue). We note the exponential relationship between the Coulomb stress and the relative seismicity rate, consistent with the solution to the ODE described by Equation 1 (Segall and Lu, 2015). We also consider a case where we neglect the first injection and only model the second injection (black dashed line). For this case, the injection starts at the original reservoir pressure. This is to investigate the relevance of the stressing history on the seismic response. Looking at the modeled seismicity rate (right vertical axis of Figure 7), we observe that in the near-field, it becomes lower than the estimated background seismicity ($R < 1$) after the end of the first injection. This behavior is not observed in the far-field where the seismicity rate goes back to the estimated initial background value ($R = 1$ at the end of the first injection). The low seismicity rate in the near-field is likely due to the continuous post-injection pressure decrease resulting in a negative pressure rate (Almakari et al., 2019). Interestingly, the relative seismicity rate in the near-field at the top of the fault is about one order of magnitude larger for the second injection if we neglected the first one. Nevertheless, while this local decrease in seismicity rate following the shut-in of the first injection may have contributed to the lack of recorded seismicity during the second one, its impact is negligible compared to the overall lower pressure changes acting on the faults.

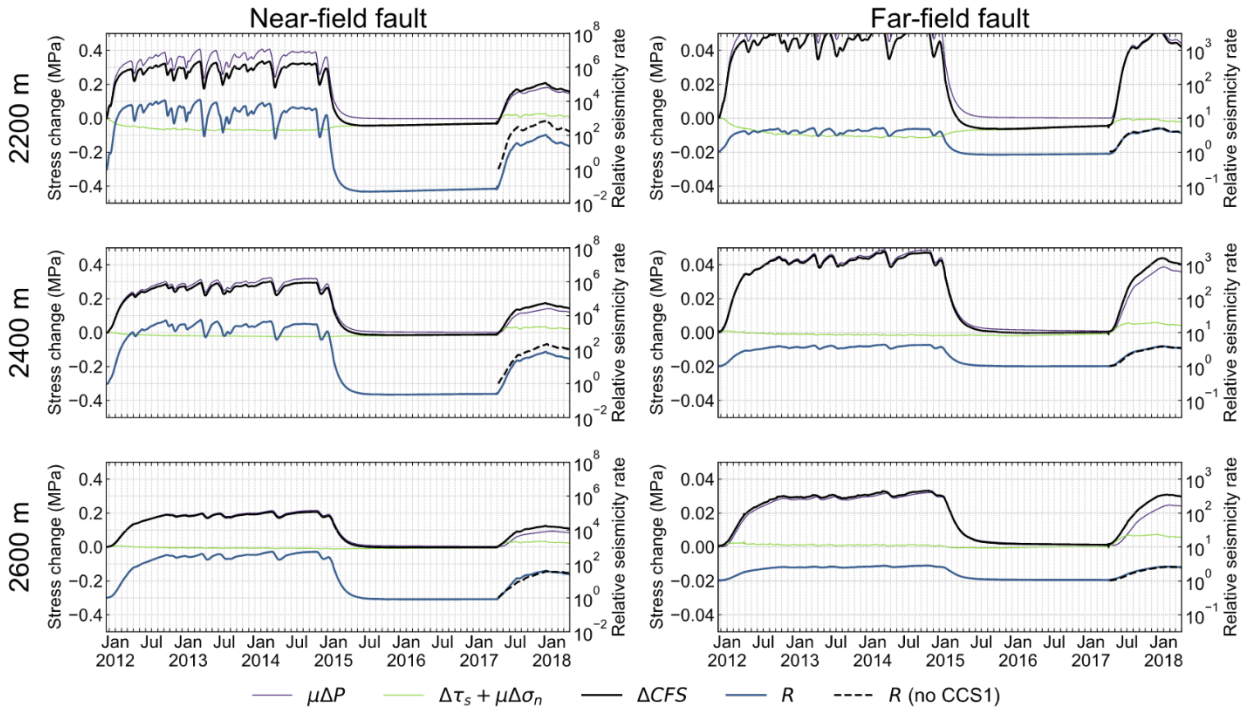

Figure 7. Calculated Coulomb stress along with contributions of pressure and poroelastic stress changes and relative seismicity rate evolutions at selected (left-hand side) near-field and (right-hand side) far-field points. The changes in Coulomb stress, and contribution to the Coulomb stress by pressure and stress changes are represented in black, purple and green, respectively. The blue solid line corresponds to the relative seismicity rate. The black dashed line represents the relative seismicity rate during the second injection if we neglect the first injection.

1. **Effect of injection rate on seismicity rate**

For equivalent total injected volume, Barbour et al. (2017) showed that a variable injection rate may induce more seismicity compared to a constant injection rate. Here, we investigate the effect of four different injection scenarios by comparing the seismicity rate generated by our hydromechanical earthquake nucleation model for different injection rates. We note that we only simulate and compare with the injection in well CCS1 for which fluid-induced seismicity has been observed. More specifically, given a total volume of approximately one million tons injected within the span of three years, we consider a first constant injection rate at 11 kg CO_2/s (Scenario A), and a second piecewise constant injection rate increasing from 10 kg CO_2/s to 12 kg CO_2/s (Scenario B). For both rates, in Scenarios C and D, we also consider a variant with two-week shut-in phases every six months (equivalent to the longest shut-in period during in-

jection in CCS1). Figure 8 shows the seismicity rates and annual magnitude probabilities of exceedance for the four injection rates using a b-value of $b = 1.1$ (Bauer et al., 2016), and a minimum and maximum magnitudes of $M_{\min} = -0.7$ and $M_{\max} = 4$. Figure 9 shows the same annual magnitude probabilities of exceedance as Figure 8 with the results displayed for each year. The seismicity rate and magnitude of exceedance probability modeled for the first injection in well CCS1 are also displayed for comparison. For the reference case, the probability for exceeding M2 is 24%, 21% and 18% in 2012, 2013 and 2014, respectively. For Scenario A, most seismicity occurs at the beginning of the injection and decreases over time resulting in a higher probability for exceeding M2 in 2012 (32%). For Scenario B, the seismicity rate steadily increases up to a maximum of 0.9 events/day and followed by a steady decrease, annual probabilities for exceeding M2 are similar throughout the injection (about 22%). Scenarios C and D show that the shut-in phases induce an immediate drop in the seismicity rate, followed by a larger seismicity rate increase when the injection restarts, compared to scenarios A and B. This behavior is also observed in the reference case where long shut-in phases (e.g., March 2013, February 2014, October 2014) yield an instantaneous drop in seismicity rate which subsequently increases with a time lag. Yet, annual probabilities for exceeding M2 are only slightly lower for both Scenarios C and D. Overall, in our model, we observe a correlation between the injection rate and the modeled seismicity rate for which the response appears to depend on the amplitude variations of the injection rate.

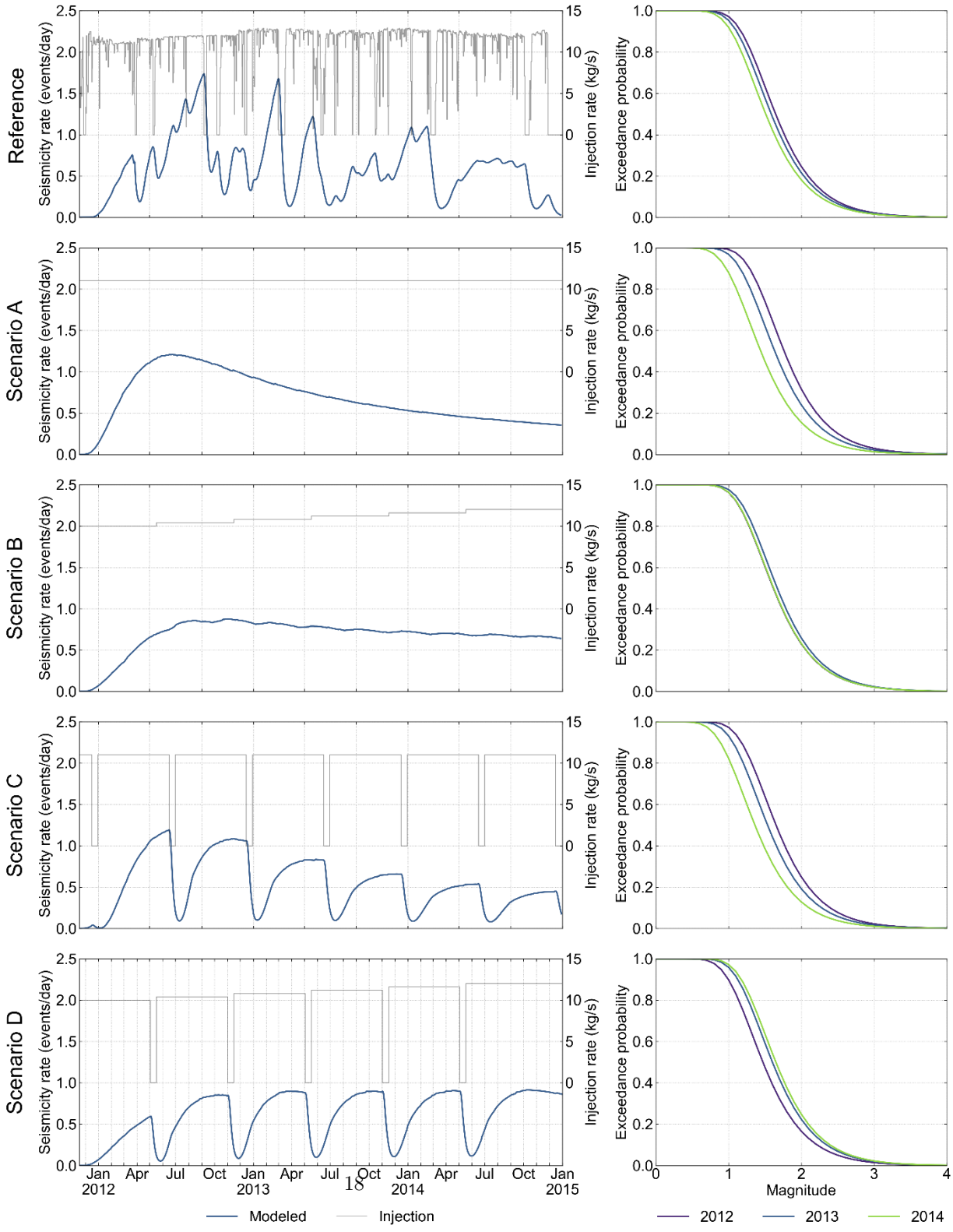
Reference
Scenario A
Scenario B
Scenario C
Scenario D
Seismicity rate (events/day)
Injection rate (kg/s)
Exceedance probability
Jan 2012
Apr
Jul
Oct
Jan 2013
Apr
Jul
Oct
Jan 2014
Apr
Jul
Oct
Jan 2015
Magnitude
Modeled
Injection
2012
2013
2014

Figure 8. Modeled seismicity rate (blue solid line) for different injection rates (left-hand side). The injection rate is represented by the thin gray solid line. Annual magnitude probability of exceedance (right-hand side).

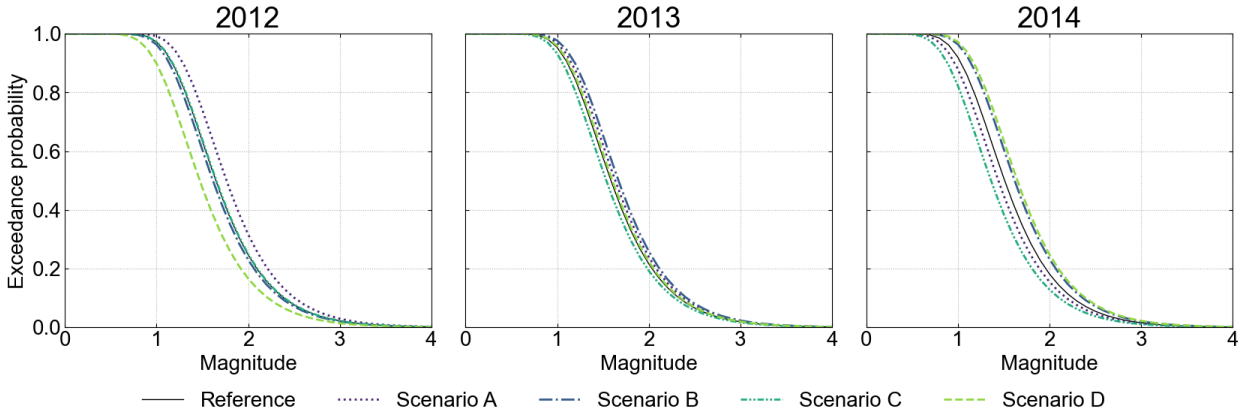

Figure 9. Annual magnitude probability of exceedance for different injection rates sorted by year.

1. Discussion and conclusion

In this paper, we modeled the seismicity induced along the Precambrian basement faults by the two CO_2 injection wells at Decatur Illinois, specifically wells CCS1 and CCS2 from November 2011 to April 2018. Our coupled hydromechanical model reproduces characteristic features of the observed microseismic activity. The modeled seismicity rates are comparable to recorded seismicity in terms of onset timings and peak rate amplitudes for the first injection, while modeled seismicity is negligible for the second injection consistent with field observations. Our modeling results suggest that the seismicity at Decatur is strongly influenced by pressure effects. However, modeling of injection in CCS1 indicates that poroelastic stresses are not negligible and tend to impede reactivation, in particular in the vicinity of the injection wells. Because the seismicity rates forecast by the rate-and-state earthquake nucleation model are exponentially related to the pressure and poroelastic stress rates, ignoring poroelastic effects (i.e., only flow modeling and using $\Delta CFS = \mu \Delta P$) would overpredict the seismicity rate by approximately one order of magnitude according to our model (using the same parameters for rate-and-state simulation). This result highlights the necessity of coupled hydromechanical modeling to accurately capture the main physical processes related to fluid-induced seismicity, in agreement with recent studies (Barbour et al., 2017; Chang and Segall, 2016; Fan et al., 2019; Zhai et al., 2019).

In addition, the rate-and-state model used in this study estimates the induced seismicity rate relatively to the background seismicity rate. Due to the lack of earthquake with magnitude $M \geq -0.7$ recorded prior to the injection, we could

not derive a background seismicity rate based on recorded data. Hence, we calibrated the background seismicity rate along with the constitutive parameter to match the observed seismicity rate. The background seismicity rate has been calibrated for comparison purpose and the inverted value is fairly uncertain (see SI, Section S1). An analysis of the sensitivity of the seismicity rate with respect to the background seismicity rate shows that modeled seismicity rates would fit the observed seismicity rate comparably well for background seismicity rates ranging between 0.3 and 0.6 events/year. Outside this range, the main peak amplitudes of the earthquake sequence are not properly captured. Given these uncertainties on the background seismicity rate, the modeled seismicity rates shown in this work must be interpreted within the context of a probabilistic analysis (Barbour et al., 2017). Nevertheless, regardless of the value of the background seismicity rate, our numerical model shows that the seismicity rate after the end of the first injection becomes lower than the initial background seismicity rate ($R < 1$), in particular near the injection well CCS1. Similar results have been observed in other modeling studies (Almakari et al., 2019) and is linked to negative pressure rates as the pressure is diffusing out of the faults. Due to the stressing history, seismicity rates forecast for the second injection are lower than if we had ignored the first injection phase. Nevertheless, despite the higher injection rate, the modeled pressure changes induced by the second injection on the basement faults are significantly lower which indicates that the absence of observed seismicity during the second phase is principally due to the injection zone in the CCS2 well location above the low permeability mudstone layer and the higher porosity and permeability in CCS2 injection zone relative to the CCS1 injection zone (Williams-Stroud et al., 2020).

We note that our model domain is fairly simple and consists of a three-dimensional layer-cake model that only includes vertical basement faults inferred from the observed microseismic clusters. Structural faults interpreted in the 3D seismic volume that could potentially impede pressure diffusion have not been modeled. For the sake of simplicity, we also assumed that the basement faults are merely hydraulically connected to the lower part of the reservoir, but do not vertically extend across it. Additionally, we only considered a homogeneous set of faults with invariable permeability. Several numerical simulations have demonstrated that location and timing of fluid-induced seismicity is affected by the variations of fault permeability (Chang and Segall, 2016; Zhang et al., 2013). Besides, we considered the rate-and-state parameters to also be homogeneous across the area of study. All these simplifications yield some discrepancies between the model outputs and the observations. For example, in our model, seismicity initiates at the top of the faults and propagates downward into the basement, while in some clusters, the observed seismicity starts within the basement. Despite these disagreements and the low complexity of our model, it is able to reproduce the principal features of the earthquake sequence recorded at the site, implying that the main physical processes involved are captured by our model.

Finally, we used our coupled hydromechanical earthquake nucleation model to

study the effect of different injection scenarios on the seismicity rate, assuming equivalent total injected volumes of CO_2. We found a correlation between the injection rate and the modeled seismicity rate. More precisely, seismicity rate immediately decreases in response to a shut-in phase and increases with a time lag when the injection restarts, the peak amplitude of the seismicity rate depending on the amplitude of the injection rate increase. However, we did not find significant changes in terms of modeled seismicity (total number of events and magnitude probability of exceedance) between the few scenarios tested and the actual injection rate, which can be explained by the already fairly constant injection rate used for the first injection in well CCS1. Additional studies are being planned to improve the model by considering heterogeneity in several model parameters and to identify factors leading to more accurate characterization of the risk of inducing earthquakes in GCS activities.

Data and resources

The induced seismicity catalog (2019 version) and injection data used in this work were acquired by the Illinois State Geological Survey under projects funded by the U.S. Department of Energy through the National Energy Technology Laboratory. The three-dimensional computational mesh is generated using the open-source meshing software LaGriT. Hydromechanical properties are taken from published literature. The numerical simulations are carried out using TOUGH3-FLAC. TOUGH3 is a fluid-flow numerical simulator developed at Lawrence Berkeley National Laboratory and FLAC3D is a geomechanical simulator commercialized by Itasca Inc. Rate-and-state seismicity modeling, earthquake catalog declustering and optimization codes are written in Python.

Acknowledgements

We thank Sherilyn Williams-Stroud, Robert Bauer and Sallie Greenberg, Illinois State Geological Survey (ISGS) Illinois Basin - Decatur Project, for helpful discussions and reviews of an earlier draft. This work was supported by TotalEnergies E&P Recherche et Développement and by Lawrence Berkeley National Laboratory under Department of Energy Contract No. DE-AC02-05CH11231.

Nomenclature

Symbol	Definition	Unit
Declustering		
d	Fractal dimension of earthquake epicenters	
m_i	Magnitude of earthquake i	
r_{ij}	Euclidean interevent distance	km
R_{ij}	Rescaled distance	
t_{ij}	Interevent time	year
T_{ij}	Rescaled time	
w	Weighting coefficient	
η_{ij}	Nearest-neighbor proximity	
η_0	Nearest-neighbor proximity cutoff threshold	

Symbol	Definition	Unit
Reservoir model		
C_p	Pore compressibility	Pa^{-1}
E	Young's modulus	Pa
G	Shear modulus	Pa
K_h, K_v	Permeability (horizontal and vertical)	mD
V_p, V_s	Velocity (P- and S-wave)	m/s
α	Biot's coefficient	
θ	Fault dip angle	°
ν	Poisson's ratio	
ρ	Density	kg/m^3
σ_v, σ_H, σ_h	Principal stress (vertical, max. and min. horizontal)	Pa or Pa/m
ϕ	Porosity	
Seismicity model		
A	Rate-and-state constitutive parameter	Pa
b	b-value	
M	Magnitude of earthquake	
M_c	Magnitude of completeness	
r, r_0	Seismicity rate (absolute and background)	event/day
R	Relative seismicity rate	
ΔCFS	Coulomb stress change	Pa
ΔP	Pore pressure change	Pa
$\Delta\sigma_n$	Normal stress change	Pa
$\Delta\tau_s$	Shear stress change	Pa
μ	Friction coefficient	
$\dot{\tau}$, $\dot{\tau_0}$	Stressing rate (absolute and background)	Pa/day
van Genuchten model		
$P_{\max}$	Maximum capillary pressure	Pa
S_{gr}	Residual gas saturation	
S_{lr}	Residual liquid saturation	
S_{ls}	Saturated liquid content	
λ	Fitting parameter	

References

Almakari, M., Dublanchet, P., Chauris, H., & Pellet, F. (2019). Effect of the Injection Scenario on the Rate and Magnitude Content of Injection-Induced Seismicity: Case of a Heterogeneous Fault. *Journal of Geophysical Research: Solid Earth*, *1*, 1–23. https://doi.org/10.1029/2019jb017898Auger, A. (2016). *Analysis of Comparison-based Stochastic Continuous Black-Box Optimization Algorithms* [PhD Thesis]. Université Paris-Sud.Barbour, A. J., Norbeck, J. H., & Rubinstein, J. L. (2017). The Effects of Varying Injection Rates in Osage County, Oklahoma, on the 2016 Mw 5.8 Pawnee Earthquake. *Seismological Research Letters*, *88*(4), 1040–1053. https://doi.org/10.1785/0220170003Bauer, R. A., Carney, M., & Finley, R. J. (2016). Overview of microseismic response to

CO2 injection into the Mt. Simon saline reservoir at the Illinois Basin-Decatur Project. *International Journal of Greenhouse Gas Control*, *54*, 378–388. https://doi.org/10.1016/j.ijggc.2015.12.015Benson, S. M., & Cole, D. R. (2008). CO2 Sequestration in Deep Sedimentary Formations. *Elements*, *4*(5), 325–331. https://doi.org/10.2113/gselements.4.5.325Cappa, F., & Rutqvist, J. (2011). Impact of CO2 geological sequestration on the nucleation of earthquakes. *Geophysical Research Letters*, *38*(17). https://doi.org/10.1029/2011GL048487Celia, M. A. (2017). Geological storage of captured carbon dioxide as a large-scale carbon mitigation option. *Water Resources Research*, *53*(5), 3527–3533. https://doi.org/10.1002/2017WR020841Chang, K. W., & Segall, P. (2016). Injection-induced seismicity on basement faults including poroelastic stressing. *Journal of Geophysical Research: Solid Earth*, *121*(4), 2708–2726. https://doi.org/10.1002/2015JB012561Choy, G. L., Rubinstein, J. L., Yeck, W. L., McNamara, D. E., Mueller, C. S., & Boyd, O. S. (2016). A rare moderate-sized (M w 4.9) earthquake in Kansas: Rupture process of the Milan, Kansas, earthquake of 12 November 2014 and its relationship to fluid injection. *Seismological Research Letters*, *87*(6), 1433–1441.Deichmann, N., & Giardini, D. (2009). Earthquakes Induced by the Stimulation of an Enhanced Geothermal System below Basel (Switzerland). *Seismological Research Letters*, *80*(5), 784–798. https://doi.org/10.1785/gssrl.80.5.784Dieterich, J. (1994). A constitutive law for rate of earthquake production and its application to earthquake clustering. *Journal of Geophysical Research: Solid Earth*, *99*(B2), 2601–2618. https://doi.org/10.1029/93JB02581Ellsworth, W. L., Llenos, A. L., McGarr, A. F., Michael, A. J., Rubinstein, J. L., Mueller, C. S., Petersen, M. D., & Calais, E. (2015). Increasing seismicity in the US midcontinent: Implications for earthquake hazard. *The Leading Edge*, *34*(6), 618–626.Ester, M., Kriegel, H.-P., Sander, J., & Xu, X. (1996). *A density-based algorithm for discovering clusters in large spatial databases with noise. 96*(34), 226–231.Fan, Z., Eichhubl, P., & Newell, P. (2019). Basement Fault Reactivation by Fluid Injection Into Sedimentary Reservoirs: Poroelastic Effects. *Journal of Geophysical Research*, 16.Fehlberg, E. (1969). *Low-order classical Runge-Kutta formulas with stepsize control and their application to some heat transfer problems* (Vol. 315). National Aeronautics and Space Administration.Finley, R. J. (2014). An overview of the Illinois Basin – Decatur Project. *Greenhouse Gases: Science and Technology*, *4*(5), 571–579. https://doi.org/10.1002/ghg.1433Genuchten, M. T. van. (1980). A Closed-form Equation for Predicting the Hydraulic Conductivity of Unsaturated Soils. *Soil Science Society of America Journal*, *44*(5), 892–898. https://doi.org/10.2136/sssaj1980.03615995004400050002xGoertz-Allmann, B. P., Gibbons, S. J., Oye, V., Bauer, R., & Will, R. (2017). Characterization of induced seismicity patterns derived from internal structure in event clusters. *Journal of Geophysical Research: Solid Earth*, *122*(5), 3875–3894. https://doi.org/10.1002/2016JB013731Hakimhashemi, A. H., Schoenball, M., Heidbach, O., Zang, A., & Grünthal, G. (2014). Forward modelling of seismicity rate changes in georeservoirs with a hybrid geomechanical-statistical prototype model. *Geothermics*, *52*, 185–194. https://doi.org/10.1016/j.geothermics.2014.01.001Hamburger, M., Galgana,

G., Johnson, K., Pavlis, G., & Shoemaker, K. (2010). *Observational and Geodynamic Constraints on Active Deformation in the Southern Illinois Basin.pdf* (p. 24). Department of Geological Sciences, Indiana University, Bloomington, IN 47405.Hansen, N., & Ostermeier, A. (2001). Completely Derandomized Self-Adaptation in Evolution Strategies. *Evolutionary Computation*, *9*(2), 159–195. https://doi.org/10.1162/106365601750190398Hombach, M., DeShon, H., Ellsworth, W., Stump, B., Hayward, C., Frohlich, C., Oldham, H., Olson, J., Magnani, M., & Brokaw, C. (2015). Causal factors for seismicity near Azle. *Texas. Nat.*Jha, B., & Juanes, R. (2014). Coupled multiphase flow and poromechanics: A computational model of pore pressure effects on fault slip and earthquake triggering. *Water Resources Research*, *50*(5), 3776–3808. https://doi.org/10.1002/2013WR015175Jung, Y., Pau, G. S. H., Finsterle, S., & Pollyea, R. M. (2017). TOUGH3: A new efficient version of the TOUGH suite of multiphase flow and transport simulators. *Computers & Geosciences*, *108*, 2–7. https://doi.org/10.1016/j.cageo.2016.09.009Kaven, J. O., Hickman, S. H., McGarr, A. F., & Ellsworth, W. L. (2015). Surface Monitoring of Microseismicity at the Decatur, Illinois, CO2 Sequestration Demonstration Site. *Seismological Research Letters*, *86*(4), 1096–1101. https://doi.org/10.1785/0220150062Keranen, K. M., Weingarten, M., Abers, G. A., Bekins, B. A., & Ge, S. (2014). Sharp increase in central Oklahoma seismicity since 2008 induced by massive wastewater injection. *Science*, *345*(6195), 448–451.Laurent, J., Bouteca, M. J., Sarda, J.-P., & Bary, D. (1993). Pore-pressure influence in the poroelastic behavior of rocks: Experimental studies and results. *SPE Formation Evaluation*, *8*(02), 117–122.Mehnert, E., Damico, J. R., Grigsby, N. P., Monson, C. C., Patterson, C. G., & Yang, F. (2019). Geologic Carbon Sequestration in the Illinois Basin: Numerical Modeling to Evaluate Potential Impacts. *Illinois State Geological Survey*, *598*, 71.Metz, B., Davidson, O., & De Coninck, H. (2005). *Carbon dioxide capture and storage: Special report of the intergovernmental panel on climate change*. Cambridge University Press.Myer, L. R., & Daley, T. M. (2011). Elements of a best practices approach to induced seismicity in geologic storage. *Energy Procedia*, *4*, 3707–3713. https://doi.org/10.1016/j.egypro.2011.02.303Navas-Portella, V., Jiménez, A., & Corral, Á. (2020). No Significant Effect of Coulomb Stress on the Gutenberg-Richter Law after the Landers Earthquake. *Scientific Reports*, *10*(1), 2901. https://doi.org/10.1038/s41598-020-59416-2Norbeck, J. H., & Rubinstein, J. L. (2018). Hydromechanical Earthquake Nucleation Model Forecasts Onset, Peak, and Falling Rates of Induced Seismicity in Oklahoma and Kansas. *Geophysical Research Letters*, *45*(7), 2963–2975. https://doi.org/10.1002/2017GL076562Rinaldi, A. P., Rutqvist, J., Luu, K., Blanco-Martín, L., Hu, M., & Sentís, M. L. (2021). *TOUGH3-FLAC3D: A Modeling Approach for Parallel Computing of Fluid Flow and Geomechanics* [Preprint]. Informatics. https://doi.org/10.1002/essoar.10505967.1Rutqvist, J. (2011). Status of the TOUGH-FLAC simulator and recent applications related to coupled fluid flow and crustal deformations. *Computers & Geosciences*, *37*(6), 739–750. https://doi.org/10.1016/j.cageo.2010.08.006Rutqvist, J. (2012). The Geomechanics of CO2 Storage in Deep Sedimentary Formations. *Geotechnical*

and Geological Engineering, *30*(3), 525–551. https://doi.org/10.1007/s10706-011-9491-0Rutqvist, J., Rinaldi, A. P., Cappa, F., Jeanne, P., Mazzoldi, A., Urpi, L., Guglielmi, Y., & Vilarrasa, V. (2016). Fault activation and induced seismicity in geological carbon storage—Lessons learned from recent modeling studies. *Journal of Rock Mechanics and Geotechnical Engineering*, *8*(6), 789–804. https://doi.org/10.1016/j.jrmge.2016.09.001Rutqvist, J., Wu, Y.-S., Tsang, C.-F., & Bodvarsson, G. (2002). A modeling approach for analysis of coupled multiphase fluid flow, heat transfer, and deformation in fractured porous rock. *International Journal of Rock Mechanics and Mining Sciences*, *39*(4), 429–442. https://doi.org/10.1016/S1365-1609(02)00022-9Schoenball, M., Davatzes, N. C., & Glen, J. M. G. (2015). Differentiating induced and natural seismicity using space-time-magnitude statistics applied to the Coso Geothermal field. *Geophysical Research Letters*, *42*(15), 6221–6228. https://doi.org/10.1002/2015GL064772Schoenball, M., & Ellsworth, W. L. (2017). A Systematic Assessment of the Spatiotemporal Evolution of Fault Activation Through Induced Seismicity in Oklahoma and Southern Kansas. *Journal of Geophysical Research: Solid Earth*, *122*(12), 10,189-10,206. https://doi.org/10.1002/2017JB014850Segall, P., & Lu, S. (2015). Injection-induced seismicity: Poroelastic and earthquake nucleation effects. *Journal of Geophysical Research: Solid Earth*, *120*, 5082–5103. https://doi.org/10.1002/2015JB012060.ReceivedSenel, O., Will, R., & Butsch, R. J. (2014). Integrated reservoir modeling at the Illinois Basin—Decatur Project. *Greenhouse Gases: Science and Technology*, *4*(5), 662–684. https://doi.org/10.1002/ghg.1451Settari, A., Bachman, R., & Walters, D. (2005). *How to approximate effects of geomechanics in conventional reservoir simulation*. SPE annual technical conference and exhibition.Siggins, A. (2010). *Passive microseismic monitoring at an Australian CO2 geological storage site*. *12*, 7636.Smith, V., & Jaques, P. (2016). Illinois Basin – Decatur Project pre-injection microseismic analysis. *International Journal of Greenhouse Gas Control*, *54*, 362–377. https://doi.org/10.1016/j.ijggc.2015.12.004Strandli, C. W., Mehnert, E., & Benson, S. M. (2014). CO2 Plume Tracking and History Matching Using Multilevel Pressure Monitoring at the Illinois Basin – Decatur Project. *Energy Procedia*, *63*, 4473–4484. https://doi.org/10.1016/j.egypro.2014.11.483Townend, J., & Zoback, M. D. (2000). How faulting keeps the crust strong. *Geology*, *28*(5), 399–402. https://doi.org/10.1130/0091-7613(2000)28<399:HFKTCS>2.0.CO;2Verdon, J. P., Stork, A. L., Bissell, R. C., Bond, C. E., & Werner, M. J. (2015). Simulation of seismic events induced by CO2 injection at In Salah, Algeria. *Earth and Planetary Science Letters*, *426*, 118–129.Vilarrasa, V., Carrera, J., Olivella, S., Rutqvist, J., & Laloui, L. (2019). Induced seismicity in geologic carbon storage. *Solid Earth*, *10*(3), 871–892. https://doi.org/10.5194/se-10-871-2019Weingarten, M., Ge, S., Godt, J. W., Bekins, B. A., & Rubinstein, J. L. (2015). High-rate injection is associated with the increase in US mid-continent seismicity. *Science*, *348*(6241), 1336–1340.Will, R., El-Kaseeh, G., Jaques, P., Carney, M., Greenberg, S., & Finley, R. (2016). Microseismic data acquisition, processing, and event characterization at the Illinois Basin

– Decatur Project. *International Journal of Greenhouse Gas Control*, *54*, 404–420. https://doi.org/10.1016/j.ijggc.2016.01.007Will, R., Smith, V., Lee, D., & Senel, O. (2016). Data integration, reservoir response, and application. *International Journal of Greenhouse Gas Control*, *54*, 389–403. https://doi.org/10.1016/j.ijggc.2015.12.020Williams-Stroud, S., Bauer, R., Leetaru, H., Oye, V., Stanek, F., Greenberg, S., & Langet, N. (2020). *Analysis of Microseismicity and Reactivated Fault Size to Assess the Potential for Felt Events by CO2 Injection in the Illinois Basin.* 17.Zaliapin, I., & Ben-Zion, Y. (2020). Earthquake Declustering Using the Nearest-Neighbor Approach in Space-Time-Magnitude Domain. *Journal of Geophysical Research: Solid Earth*, *125*(4). https://doi.org/10.1029/2018JB017120Zhai, G., Shirzaei, M., & Manga, M. (2020). Elevated Seismic Hazard in Kansas Due to High-Volume Injections in Oklahoma. *Geophysical Research Letters*, *47*(5). https://doi.org/10.1029/2019GL085705Zhai, G., Shirzaei, M., Manga, M., & Chen, X. (2019). Pore-pressure diffusion, enhanced by poroelastic stresses, controls induced seismicity in Oklahoma. *Proceedings of the National Academy of Sciences*, *116*(33), 16228–16233. https://doi.org/10.1073/pnas.1819225116Zhang, Y., Person, M., Rupp, J., Ellett, K., Celia, M. A., Gable, C. W., Bowen, B., Evans, J., Bandilla, K., Mozley, P., Dewers, T., & Elliot, T. (2013). Hydrogeologic controls on induced seismicity in crystalline basement rocks due to fluid injection into basal reservoirs. *Ground Water*, *51*(4), 525–538. https://doi.org/10.1111/gwat.12071Zoback, M. D., & Gorelick, S. M. (2012). Earthquake triggering and large-scale geologic storage of carbon dioxide. *Proceedings of the National Academy of Sciences*, *109*(26), 10164–10168. https://doi.org/10.1073/pnas.1202473109Zoback, M. L., & Zoback, M. D. (1989). Chapter 24: Tectonic stress field of the continental United States. In *Geological Society of America Memoirs* (Vol. 172, pp. 523–540). Geological Society of America. https://doi.org/10.1130/MEM172-p523

Appendix A. Calibration of hydromechanical model parameters

We history-matched hydrological model parameters against multilevel pressure data and saturation profiles measured at verification well VW1 located approximately 300 m away from injection well CCS1 (see Figure 1, right-hand side). We inverted porosities and permeabilities of layers Mount Simon A-upper through Argenta by minimizing the joint objective function defined by Equation A1, written

$$E\left(\mathbf{m}\right) = w_p \left(\mathbf{d_p^{obs}} - g_p\left(\mathbf{m}\right)\right)^\top \left(\mathbf{d_p^{obs}} - g_p\left(\mathbf{m}\right)\right) + w_s \left(\mathbf{d_s^{obs}} - g_s\left(\mathbf{m}\right)\right)^\top \left(\mathbf{d_s^{obs}} - g_s\left(\mathbf{m}\right)\right) \quad \text{(A1)}$$

where $\mathbf{m}$ is the vector of model parameters to invert (porosities and permeabilities of layers), subscripts p and s respectively denote pressure and saturation, $\mathbf{d_p^{obs}}$ and $\mathbf{d_s^{obs}}$ are the measured data vectors to history-match, and $g_p\left(\mathbf{m}\right)$ and $g_s\left(\mathbf{m}\right)$ the data vectors calculated by the forward operator g. w_p and w_s are coefficients that weigh the contributions of each dataset to the joint objective function, and are arbitrarily set to 1 and 2, respectively (with pressure expressed in MPa). The objective function is optimized using the CMA-ES (Hansen and Ostermeier, 2001) which is known to be a robust stochastic global optimization

algorithm, especially when the number of parameters to invert is relatively high (Auger, 2016). For the CMA-ES, we use a population size of 20 and 100 iterations, the initial means and standard deviations are summarized in Table A1.

To reduce the computational cost of the forward modeling (TOUGH3 simulation), we considered a radially symmetric layer-cake model with the same layering as our 3D computational mesh. Only the pressure data measured in the vicinity of the injection zone (zones 1 through 4) and the saturation profiles measured in March and July 2012 are inverted. Results of the history matching for the best fit model are represented in Figure A1.

Poisson's ratio, bulk modulus, Biot's coefficient and pore compressibility are calculated using mechanical conversion functions or empirical models (see Table A2). Figure A2 shows the pressure change front and CO_2 plume modeled for March 2012 using the 3D geomechanical model with porosity and permeability values inverted using the radial layered mesh.

Table A1. Initial means and standard deviations for the CMA-ES of each model parameter. Permeability values (horizontal and ratio) are given as $\log_{10}$ with permeability expressed in m^2.

Layer	**Parameter**	**Initial mean**	**Initial std.**
Mount Simon A-upper	Horizontal permeability	-13.5	0.2
	H/V permeability ratio	2.0	0.2
Baffle	Permeability	-15.0	0.2
Mount Simon A-lower-1	Horizontal permeability	-13.0	0.2
	H/V permeability ratio	3.5	0.2
	Porosity	0.15	0.02
Mount Simon A-lower-2	Horizontal permeability	-13.0	0.2
	H/V permeability ratio	3.0	0.2
	Porosity	0.22	0.02
Mount Simon A-lower-3	Horizontal permeability	-13.0	0.2
	H/V permeability ratio	2.0	0.2
	Porosity	0.15	0.02
Argenta	Horizontal permeability	15.0	0.2
	H/V permeability ratio	2.0	0.2

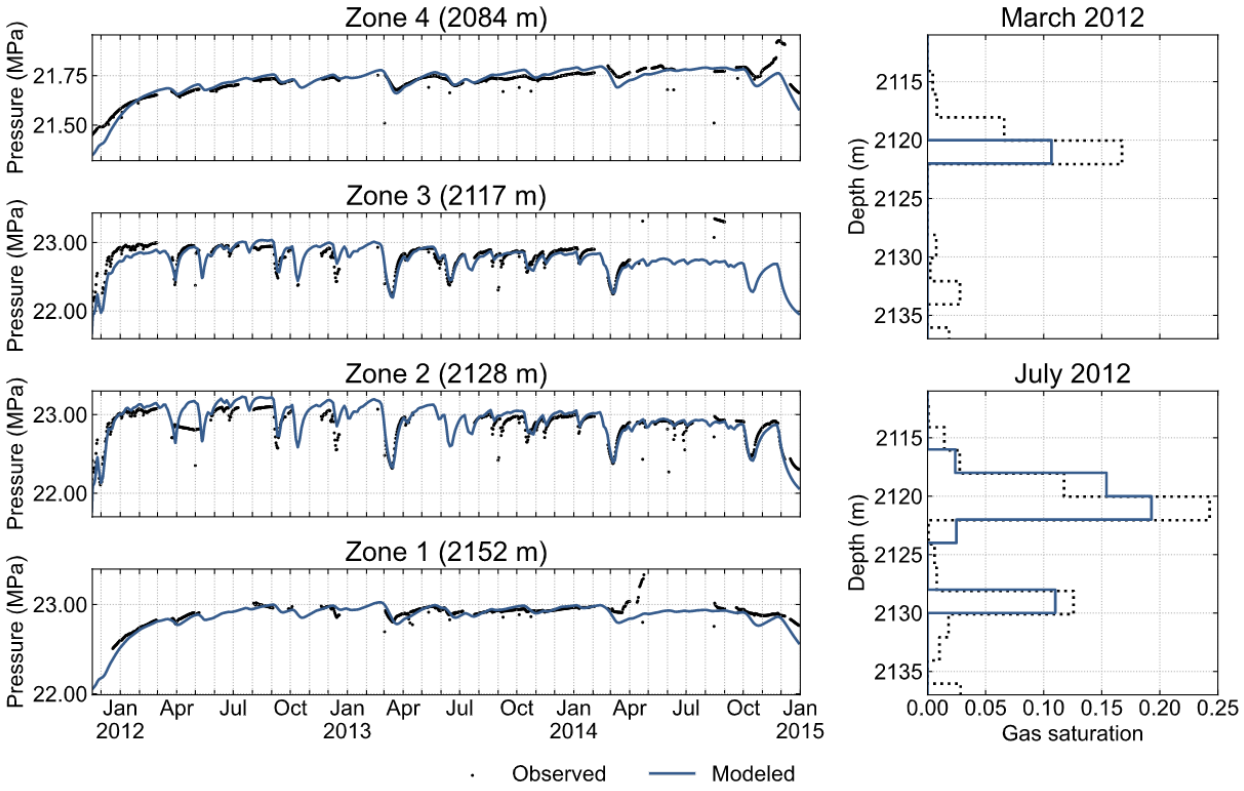

Figure A1. (Left-hand side) History-matched and modeled pressure data for zones 1 to 4. (Right-hand side) History-matched and modeled saturation profiles for March and July 2012. The black dotted and blue solid lines correspond to the history-matched and modeled data, respectively.

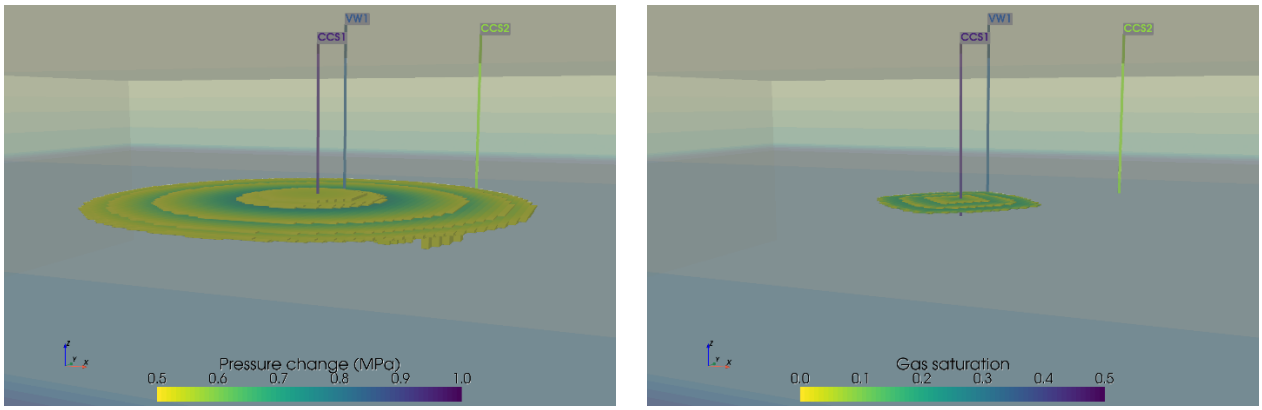

Figure A2. Modeled (left-hand side) pressure change front and (right-hand side) CO_2 plume for March 2012 using the 3D geomechanical model.

Table A2. Functions and empirical models used to calculate mechanical parameters. Young's moduli are given in Table 1.

Parameter	**Function/Empirical model**	**Reference**
Poisson's ratio (dynamic)	$\nu_{\mathrm{dyn}} = 0.5\frac{\left(\frac{V_p}{V_s}\right)^2-2}{\left(\frac{V_p}{V_s}\right)^2-1}$	
Poisson's ratio (static) 0.5_	(Will, Smith, et al., 2016)	
Bulk modulus	$K_{\mathrm{stat}} = \frac{E_{\mathrm{stat}}}{3(1-2\nu_{\mathrm{stat}})}$	
Biot's coefficient	$\alpha = 1.75\phi^{0.51}$	(Laurent et al., 1993)
Pore compressibility	$c_p = \frac{1}{K_{\mathrm{stat}}\phi}\left(1-\frac{2(1-2\nu_{\mathrm{stat}})}{3(1-\nu_{\mathrm{stat}})}\right)$	(Settari et al., 2005)